

## CHAPTER VIII

### RESULTS IN PION INDUCED REACTIONS

The previous chapters present extensive studies on the space-time geometry of the source volume and the cluster formations across the broad range of collision energies and EoS in heavy-ion collisions. We proposed the usage of space-time consideration, particularly the isospin exchange at chemical freeze-out as a tool to distinguish between thermal and coalescence models. However, we can extend our investigation beyond heavy-ion collisions at low energies as there is also a pressing need for investigations of smaller systems. Since the yield of hypertriton, for instance, demonstrates a system size dependence (Acharya et al., 2022), leading to another tension between the thermal and coalescence models. Furthermore, the hypertriton's potential use as a constraint for the coalescence parameter, hypernuclei structure, and neutron star EoS underscore the significance of probing smaller systems. In this chapter, we aim to provide supports for the realization of the coalescence mechanism as well as the theoretical predictions and insights for future experiments at smaller systems, particularly pion-induced reactions.

#### 8.1 The needs and potential of small collision systems

The interest in the low energy regime is circulating around the cluster formations (Vovchenko et al., 2020), including the quest for dark matter (Hou et al., 2017; Korsmeier et al., 2018; Doetinchem et al., 2020; Hornung, 2021; Šerkšnytė et al., 2022), the extraction of the Equation of State (EoS) for neutron stars (Capano et al., 2020; Tolos and Fabbietti, 2020; Vidaña, 2018), and the essential interplay between theoretical predictions and experimental measurements. One of the main ingredients for the EoS of neutron stars is the understanding of  $\Lambda$ N-interactions, and even  $\Lambda$ NN-interactions, as hyperons and hypernuclei are expected to be presented at the core of neutron stars (Nagels et al., 1977; Nagels et al., 1979; Shinmura et al., 1984; Fujiwara et al., 1996a; Fujiwara et al., 1996b; Nemura et al., 2000; Hildenbrand and Hammer, 2019).

Exploring these interactions can be achieved through diverse methods, including the study of correlation functions and the direct examination of bound state

formation, such as the hypertriton  ${}^3_{\Lambda}\text{H}$  made of a deuteron core with a weakly bound  $\Lambda$  (Juric et al., 1973; Abelev et al., 2010; Adam et al., 2016; Dönigus, 2013; Andronic et al., 2018). This state possesses a very small  $\Lambda$  separation energy, typically in the range of a few hundred keV (Davis, 2005; Adam et al., 2020), resulting in a wide wavefunction extending up to approximately 10 fm in radius (Braun-Munzinger and Dönigus, 2019). Notably, the size of the  ${}^3_{\Lambda}\text{H}$  wavefunction may be associated with the constraint of the coalescence parameter and the underlying  $\Lambda\text{N}$  interaction for the neutron star EoS (Nagels et al., 1977; Nagels et al., 1979; Shinmura et al., 1984; Fujiwara et al., 1996a; Fujiwara et al., 1996b; Nemura et al., 2000; Hildenbrand and Hammer, 2019).

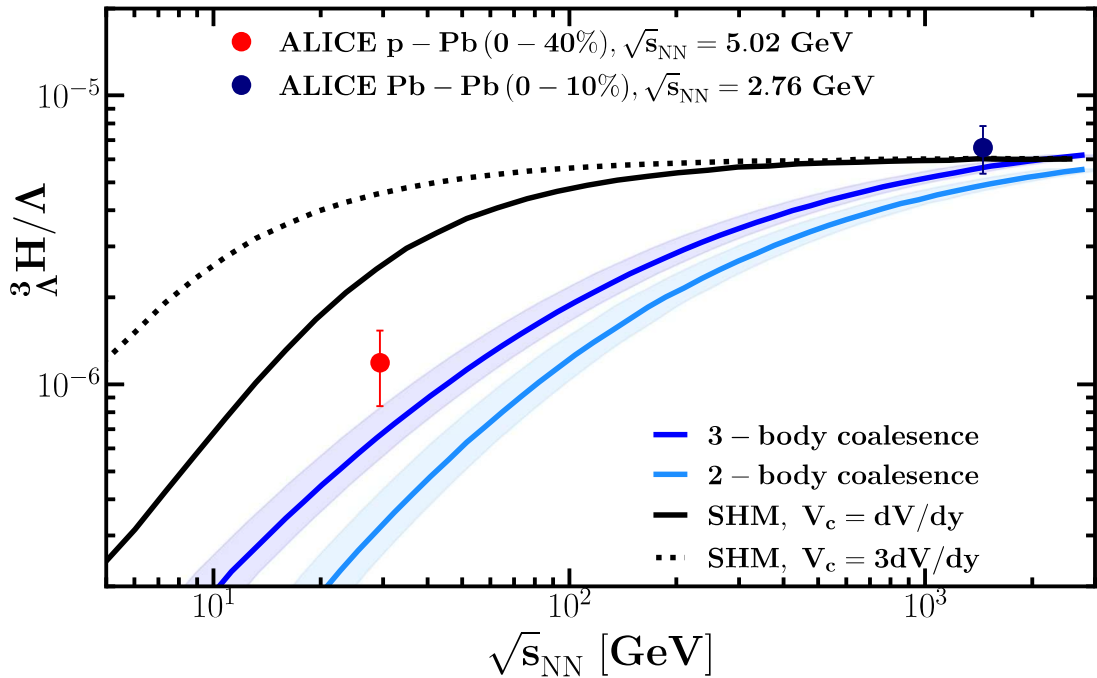


**Figure 8.1** ALICE measurements in  $p + \text{Pb}$  (in red) and  $\text{Pb} + \text{Pb}$  collisions (Adam et al., 2016) (in blue) as a function of mean charged-particle multiplicity and the predictions from canonical statistical hadronization (excluded volume) (Vovchenko et al., 2018a) and coalescence models are shown (Sun et al., 2019). The figure is adopted from Ref. (Acharya et al., 2022)

The recently published data by the ALICE experiment (Acharya et al., 2022), Fig. 8.1, of the system size dependence of  ${}^3_{\Lambda}\text{H}$  production for small collision systems in  $p+p$  and  $p+\text{Pb}$  shows that the predictions from the coalescence mechanism suppress the  ${}^3_{\Lambda}\text{H}/\Lambda$  yield compared to the results from the thermal model. The result is compared with the prediction from the canonical SHM (Vovchenko et al., 2018a), which

assumes exact conservation of baryon number, strangeness, and electric charge across a correlation volume  $V_c$ . The SHM predictions are computed using a fixed chemical freeze-out temperature of  $T_{\text{chem}} = 155$  MeV and two correlation volumes extending across one unit ( $V_c = dV/dy$ ), and three units ( $V_c = 3dV/dy$ ) of rapidity (Vovchenko et al., 2018a). The size of the correlation volume governs the influence of exact quantum number conservation, with smaller values leading to a stronger suppression of conserved charges and  $V_c \rightarrow \infty$  leading to the grand canonical ensemble. The results seem to favor the 2-body coalescence model (d-core and weakly bound  $\Lambda$ ). However, toward smaller systems, due to the limited available data, we cannot pin-point whether the hypertriton yield ratio will tend toward the thermal model prediction or the 2-body or 3-body coalescence model, thus changing the interpretation of its size and wavefunction. This again emphasizes the importance on the understanding of the cluster mechanisms and low energy studies.

Nevertheless, the new availability of secondary pion beams at the HADES experiment (Agakishiev et al., 2009) in Darmstadt, Germany, may provide a unique opportunity to study hadron and dilepton production in  $\pi + A$  interactions with a momentum of 1.7 GeV on carbon (C) and tungsten (W) targets allowing to investigate normal clusters and hypernuclei production in small systems and at low energies.

Particle production of, e.g.,  $\Lambda$  in  $p + A$  reactions results in a large forward momentum of the created particle, therefore reducing the chance for hypernuclei production (within the coalescence picture). Thus, hypernuclei will be produced outside of the nucleus. In contrast to that, pion reactions  $\pi + A$  have several advantages for cluster studies. The pion induced reaction proceeds via the excitation of a baryonic resonance,  $\pi^- + n \rightarrow \Delta^{*, -}$  or  $\Delta^- + p \rightarrow \Delta^{*, 0}$  or  $N^*$ , with a typical mass up to 2 GeV. The baryon resonance (moving forward with respect to the target system) then decays after approx. 1-2 fm/c mostly into  $\pi + N$  (leading to the production of protons and neutrons in the forward direction) and may also lead to the production of  $\Lambda$  and even  $\Xi$  via the decays  $\Lambda + K$  and  $\Xi \rightarrow KK$ , respectively (Steinheimer et al., 2017). However, the pion projectile has a larger stopping power compared to the proton beam, the production of nucleons/hyperons must be richer around the target region than the forward rapidity. Thus, one can expect the enhancement of the hypernuclei formation within the target and this allow for larger hypernuclei  $A \gg 3$  as  $\Lambda$  or  $\Xi$  inside the nucleus may slow down allowing for binding or multifragmentation into a hypernucleus. The deceleration of the hyperon will of course depend on the size of the target nucleus

and is more pronounced in the bigger tungsten than in the carbon target. Thus, the pion beam measurements at HADES provide a promising environment to explore the properties of the ( ${}^3_{\Lambda}\text{H}$ ) in small systems.

To demonstrate our arguments above and discuss the potential use of the pion beam experiment at HADES (Adamczewski-Musch et al., 2017; Yassine et al., 2023), we perform the first baseline predictions for the production of non-strange and strange clusters in  $\pi^- + \text{C}$  and  $\pi^- + \text{C}$  collisions.

To this aim, we will employ the UrQMD v3.5 with box coalescence model which has been successfully describe the production of non-strange light nuclei, i.e deuterons, tritons, helium, and strange hypertriton and further strange clusters which have not yet been measured (Gaebel et al., 2021; Hillmann et al., 2022; Reichert et al., 2023c; Reichert et al., 2023d) and then compare the results with the statistical multifragmentation approach which allows to produce (hyper)nuclei with large mass numbers relative to the system size (Botvina et al., 2021; Buyukcizmeci et al., 2020; Botvina et al., 2022; Buyukcizmeci et al., 2023).

## 8.2 Model Setup

For this study, we use the transport model UrQMD v3.5. For this analysis, the simulations are conducted in cascade mode, with potentials turned off. As a QMD-type simulation, UrQMD tracks all n-particle correlations during system evolution, preserving the collision history with detailed space-time and 4-momentum information for all particles. This data is then input into a numerical coalescence model and the Statistical Multifragmentation Model (SMM) (Bondorf et al., 1995) to compute cluster production.

All the following results are obtained by simulating 146 million and 41 million events of minimum bias  $\pi^- + \text{C}$  and  $\pi^- + \text{C}$  collisions, respectively. We define minimum bias collisions for  $\pi^- + \text{C}$  with an impact parameter range of  $0 < b < 2.5$  fm, excluding events without any interaction, and use a total cross section of  $\sigma_{\text{tot}}^{\pi^- + \text{C}} = 196.35$  mb for normalization. For  $\pi^- + \text{C}$ , we use an impact parameter range of  $0 < b < 6.5$  fm, also excluding non-interacting events, with a total cross section of  $\sigma_{\text{tot}}^{\pi^- + \text{C}} = 1327.32$  mb.

All calculations are done in the target rest frame (laboratory frame in the HADES experiment) and the rapidity  $y$  refers to this frame, i.e.  $y_{\text{target}} = 0$ . To compare with the experimental data, free  $\Lambda$  hyperons always include the  $\Sigma^0$  hyperons, as the  $\Sigma^0$  decays into a  $\Lambda$  and can not be distinguished by the experiment. However, the coales-

cence and multifragmentation routines consider only initial  $\Lambda$  hyperons, since  $\Sigma^0$  hyperons decay further away due to their comparatively long lifetime and do not significantly contribute to the hypertriton production. Protons in the simulation do not include feed down from the  $\Lambda$  decays. The units used for  $d^2\sigma/dp_T dy$  are  $[\mu\text{b}/(\text{GeV}\Delta y)]$ , and for  $d\sigma/dy$  are  $[\mu\text{b}/\Delta y]$  chosen in line with the HADES measurements (Yassine et al., 2023).

The coalescence results are evaluated at the kinetic freeze-out, while the SMM uses input from UrQMD at a fixed time in this analysis. Furthermore, all particles, as well as spectators in UrQMD, are included in the statistical multifragmentation approach. The coalescence parameter in the SMM model has been set to  $v_c = 0.22$  as this value has been shown to provide good results (Botvina et al., 2015; Buyukcizmeci et al., 2020; Botvina et al., 2021).

### 8.3 Proton and $\Lambda$ Baryon Production

We begin our exploration by investigating the double differential transverse momentum spectra of cluster constituents, i.e., protons and  $\Lambda$  hyperons.

In Fig. 8.2 (upper panel), we illustrate the double differential cross section  $d^2\sigma/dp_T dy$  in  $[\mu\text{b}/(\text{GeV}\Delta y)]$  for protons against transverse momentum across various rapidity bins (ranging from  $0 \leq y < 0.1$  to  $0.9 \leq y < 1.0$ ). For clarity, the curves are progressively scaled by factors of 10 from bottom to top. The left panel shows results for minimum bias  $\pi^- + \text{C}$  collisions, while the right panel shows results for minimum bias  $\pi^- + \text{C}$  collisions, from UrQMD (v3.5) simulations. Solid lines with symbols depict the simulated data, while open symbols represent recent HADES measurements (Yassine et al., 2023). Additionally, a dotted line denotes the exponential fit, parameterized by the yield integral and slope parameter as  $\sim C(y)p_T \sqrt{p_T^2 + m_0^2} \exp\left[-\frac{\sqrt{p_T^2 + m_0^2}}{T(y)}\right]$ , consistent with the HADES analysis (Yassine et al., 2023). The fitting to the simulation data is done within the same  $p_T$  acceptance as the HADES setup, i.e.,  $p_T \geq 0.4$  [GeV] and is displayed only for the rapidity bin  $0 \leq y < 0.1$ . Fig. 8.2 (lower panel) illustrates the relative deviation between the UrQMD simulations and the experimental data.

The simulation results demonstrate both quantitative and qualitative agreement between UrQMD model calculations of the differential cross section for protons and experimental data (open symbols) (Yassine et al., 2023) for both collision systems and across all forward rapidity bins, as well as a good match of the slope parameters between our simulations and the measured data. Notably, as anticipated, we observe

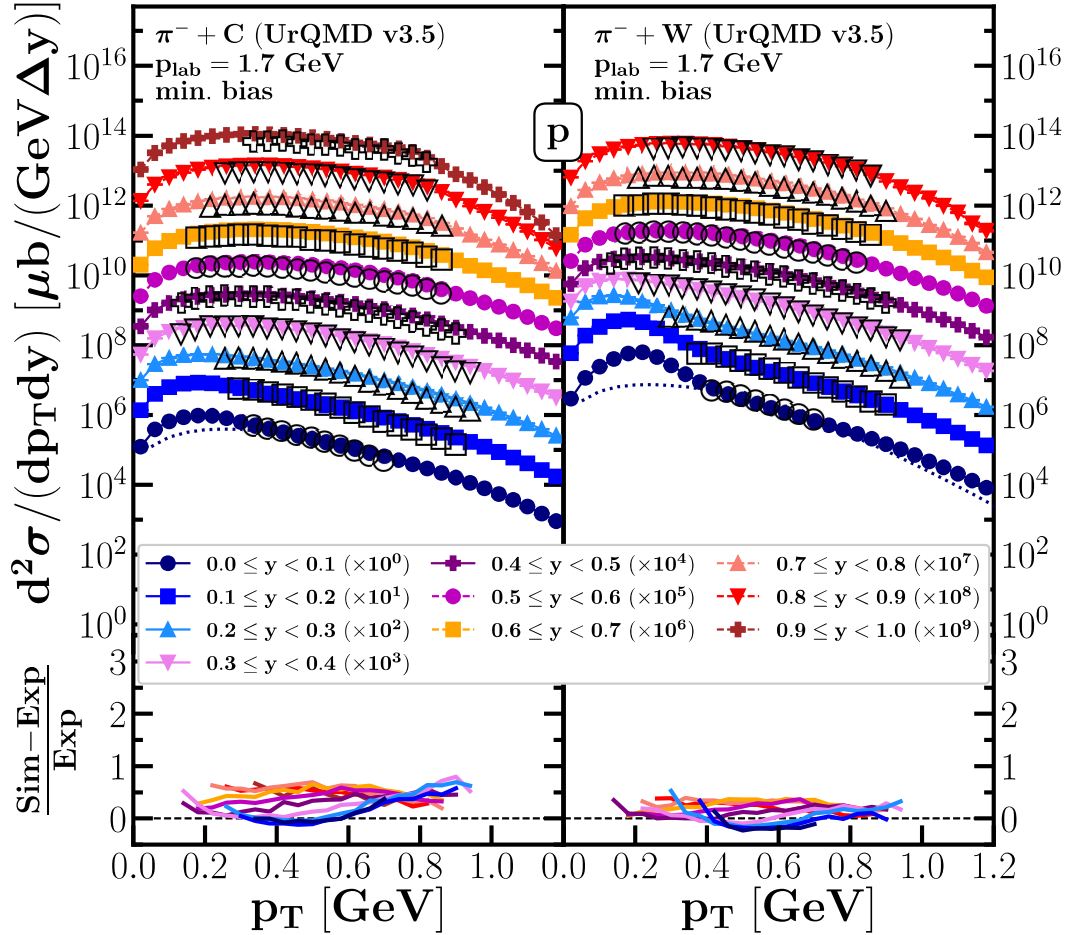


**Figure 8.2** The transverse momentum ( $p_T$ ) spectra of protons produced in minimum bias  $\pi^- + C$  (left panel) and  $\pi^- + W$  (right panel) collisions at various rapidity bins ( $0 \leq y < 0.1$  to  $0.9 \leq y < 1.0$ ) as measured by the UrQMD model (v3.5). The  $p_T$  spectra are represented by differential cross sections ( $d^2\sigma/dp_T dy$ ) in units of  $[\mu b / (\text{GeV} \Delta y)]$ . The curves for each rapidity bin are consecutively multiplied by a factor of 10 from bottom to top for better visualization. Solid lines with symbols depict the UrQMD simulation results, while open symbols represent recent HADES experimental measurements (Yassine et al., 2023). The lower panel shows the relative deviation (percentage difference) between the UrQMD simulations and the corresponding experimental data for each rapidity bin.

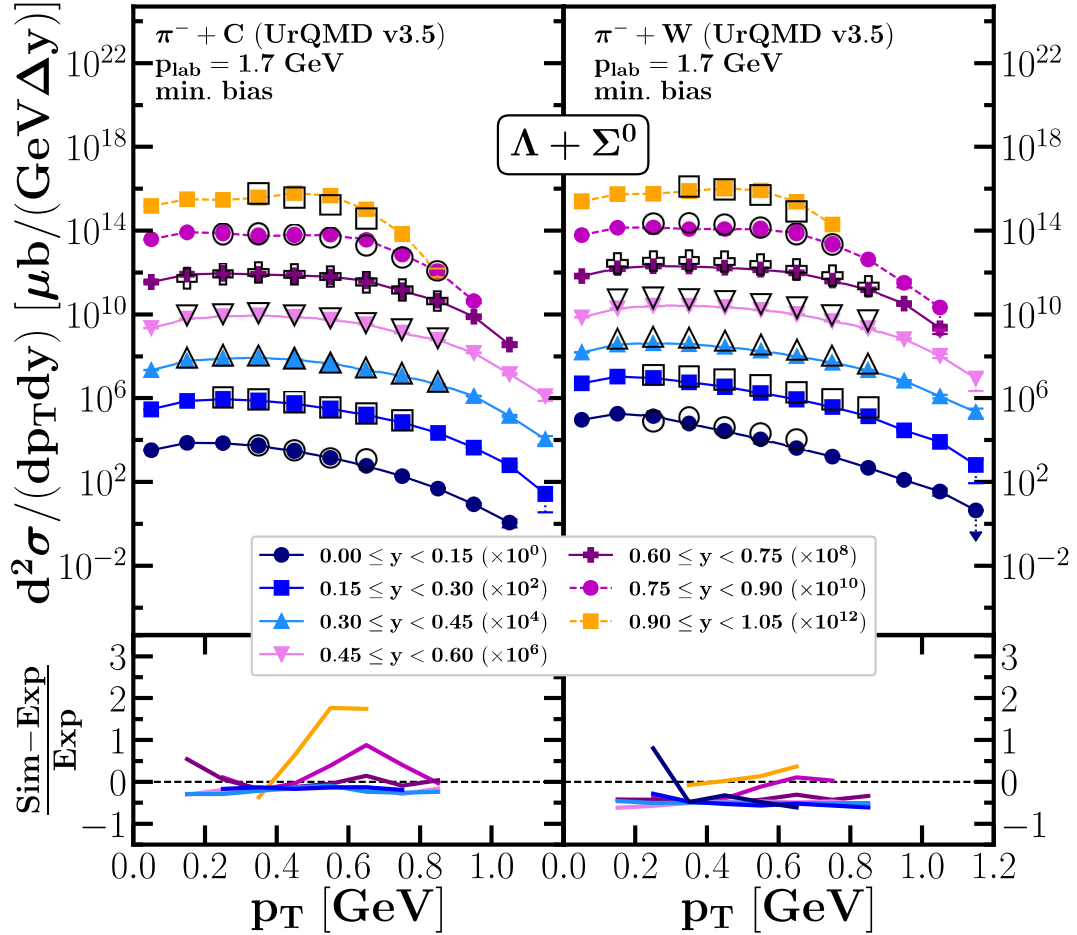


**Figure 8.3** The upper panel displays the transverse momentum ( $p_T$ ) spectra of  $\Lambda$  hyperons produced in minimum bias  $\pi^- + C$  (left) and  $\pi^- + C$  (right) collisions at various rapidity bins ( $0 \leq y < 0.15$  to  $0.9 \leq y < 1.05$ ) as calculated by the UrQMD model (v3.5). The  $p_T$  spectra are represented by differential cross sections ( $d^2\sigma/dp_T dy$ ) in units of  $[\mu\text{b}/(\text{GeV}\Delta y)]$ . The curves for each rapidity bin are consecutively multiplied by a factor of 100 for improved visualization (bottom to top). Solid lines with symbols depict the UrQMD simulations, while open symbols represent recent HADES experimental measurements (Yassine et al., 2023). The lower panel presents the relative deviation (percentage difference) between the UrQMD simulations and the corresponding experimental data for each rapidity bin

a greater proton abundance at small transverse momenta  $p_T$  in the UrQMD simulation compared to the interpolation predicted via the exponential fit function, especially at low rapidity. This arises due to limitations in the phase space coverage of the HADES detector, preventing direct observation of these residue-free protons at transverse momenta  $p_T < 0.4$  GeV around zero rapidity. This effect is evident for both systems and becomes more pronounced with increasing system size. In the subsequent section, we will demonstrate how typical extrapolation results in slight deviations in rapidity densities near  $y \approx 0$ .

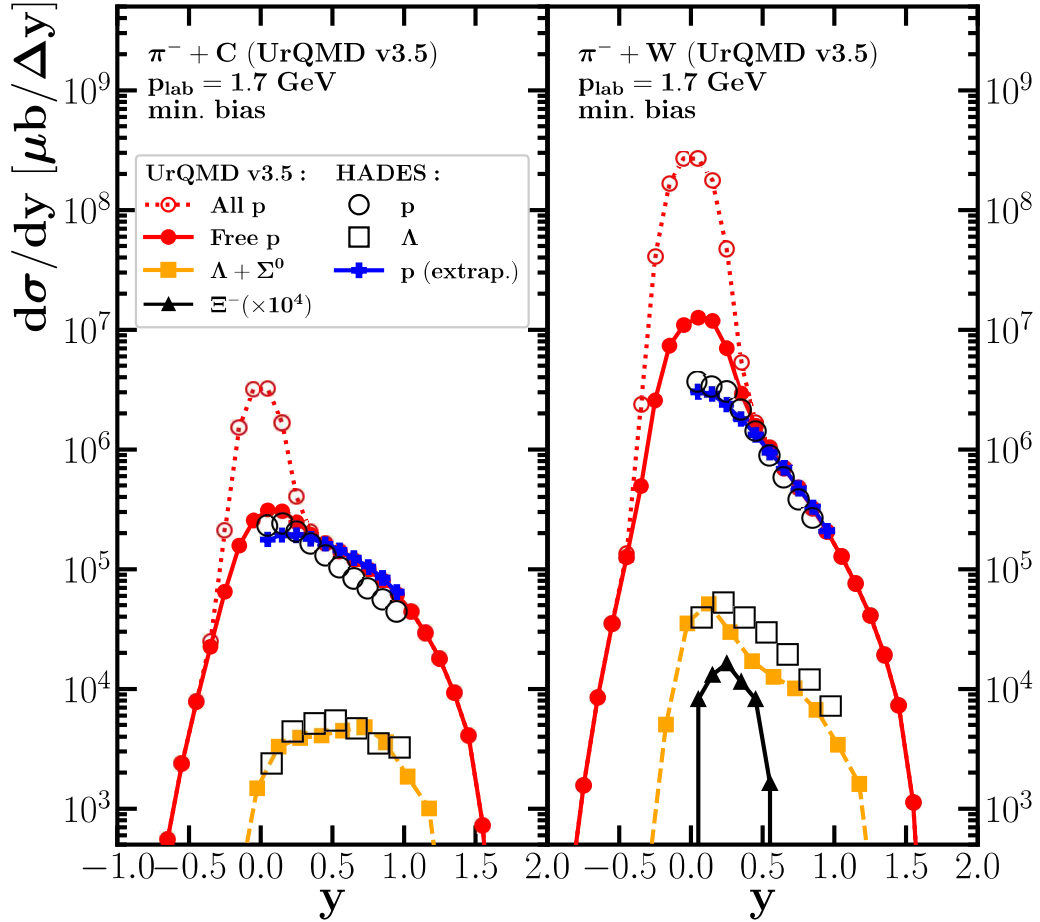
Figure 8.2 (lower panels) presents the relative differences in  $p_T$  spectra between the UrQMD (v3.5) simulation and the HADES experimental data (Yassine et al., 2023) for protons. These differences remain below 1 across the  $p_T$  range and all rapidity bins. In the carbon system, the deviations become stronger with increasing momentum and further rapidity bin. Conversely, in the tungsten system, the deviations indicate less dependence on both  $p_T$  and rapidity.

Fig. 8.3 (upper panel) shows the transverse momentum double differential cross section  $d^2\sigma/dp_T dy$  of  $\Lambda$ 's as a function of transverse momentum in different rapidity bins (from  $0 \leq y < 0.15$  to  $0.9 \leq y < 1.05$ ). The curves are scaled by factors of 100 from bottom to top for clarity. The results from minimum bias  $\pi^- + C$  and  $\pi^- + C$  collisions from UrQMD (v3.5) are presented in the left and right panels, respectively. The solid lines with symbols show the calculations and the open symbols represent the HADES measurements (Yassine et al., 2023). The relative deviation between the UrQMD simulations and experimental data is shown in the lower panel.

Similarly, the UrQMD simulations agree well with the data across the transverse momentum range in all rapidity bins. They reproduce the sharp drop-off behavior at high  $p_T$  values, a result of the limited available collision energy.

We are now able to discuss the slight deviation from using the extrapolated rapidity distribution from the exponential fit. In Fig. 8.4, we present the comparison of rapidity differential cross section spectra  $d\sigma/dy$  in  $[\mu b/\Delta y]$  of simulated protons and extrapolated protons as well as the rapidity distribution of  $\Lambda$ 's. The left panel displays the results from minimum bias  $\pi^- + C$  collisions, while the right panel displays those from minimum bias  $\pi^- + C$  collisions.

Unlike experimental approaches that rely on extrapolations from integrated transverse momentum spectra, UrQMD simulations can directly calculate particle rapidity distributions. Our results demonstrate that the extrapolated free protons obtained



**Figure 8.4** The differential cross section with respect to the rapidity  $d\sigma/dy [\mu\text{b}/\Delta y]$  of protons (red),  $\Lambda$ 's (orange), and  $\Xi$ 's (black) from minimum bias  $\pi^- + \text{C}$  (left panel) and  $\pi^- + \text{W}$  (right panel) collisions. The UrQMD results are shown as colored lines with symbols, while the open black symbols depict the recent HADES measurements (Yassine et al., 2023). The blue line with crosses shows the experimental fit function for the  $p_T$  extrapolation.

from the exponential fit (solid blue line with crosses) generally agree with the HADES data (open circles) across the measurable rapidity range. However, as mentioned earlier, there are notable limitations to this approach.

Specifically, the current exponential fit function could not account for residue free protons residing near zero rapidity (target region). These protons are unde-

tectable by the HADES experiment due to its limited coverage at nearly zero rapidity ( $p_T < 0.4$  GeV/c). The UrQMD simulations (solid red line with circles) clearly capture this effect, demonstrating a higher density of free protons around zero rapidity despite agreeing well with the exponential fit from both experimental data and simulations in the forward rapidity region. This limitation of the exponential fit extends to all protons, not just the free ones. In the target region, there are not only residue free protons but also bound protons within clusters, as depicted by the red dashed line with open circles. Additionally, the larger target nucleus, with stronger stopping power, further amplifies the presence of all protons (bounded and free protons) at zero rapidity.

The UrQMD model demonstrates its capability by successfully reproducing the measured  $\Lambda$  rapidity distributions (orange line with squares) in both  $\pi^- + C$  and  $\pi^- + C$  collision systems. This achievement indicates that the model can describe the multiplicity and general trend of  $\Lambda$  hyperons.

Furthermore, we also present the production of  $\Xi$  hyperons (black line with triangles), particularly in the  $\pi^- + C$  system. This finding, combined with the successful description of proton and  $\Lambda$  production, suggests that these low-energy, small-system collisions hold promise for studying clusters and the possibility of exploring the formation of multi-strange hyperclusters, without the need for an anti-proton beam.

## 8.4 (Light) Nuclei distributions

Building upon the successful validation of the UrQMD model in describing the production of protons,  $\Lambda$ 's, and even  $\Xi$ 's (constituents of most (hyper)nuclei), we are now well-positioned to delve into the investigation of cluster and hypernuclei formation within these collision systems.

Figure 8.5 shows the transverse momentum ( $p_T$ ) spectra of deuterons produced in minimum bias  $\pi^- + C$  (left panel) and  $\pi^- + C$  (right panel) collisions at various rapidity bins ( $0 \leq y < 0.1$  to  $0.8 \leq y < 0.9$ ) as simulated by the UrQMD model. The  $p_T$  spectra are represented by differential cross sections ( $d^2\sigma/dp_T dy$ ) in units of  $[\mu\text{b}/(\text{GeV}\Delta y)]$ . The curves for each rapidity bin are consecutively multiplied by factors of 100 (bottom to top) for improved visualization. Similar plots for tritons (Figure 8.6) and  ${}^3\text{He}$  (Figure 8.7) show the production of these light clusters across different rapidity bins ( $0 \leq y < 0.1$  to  $0.5 \leq y < 0.6$ ) in both collision systems.

The observed  $p_T$  spectra for deuterons, tritons, and  ${}^3\text{He}$  show a substantial amount of light cluster production, particularly in the target rapidity region ( $y \simeq 0$  with

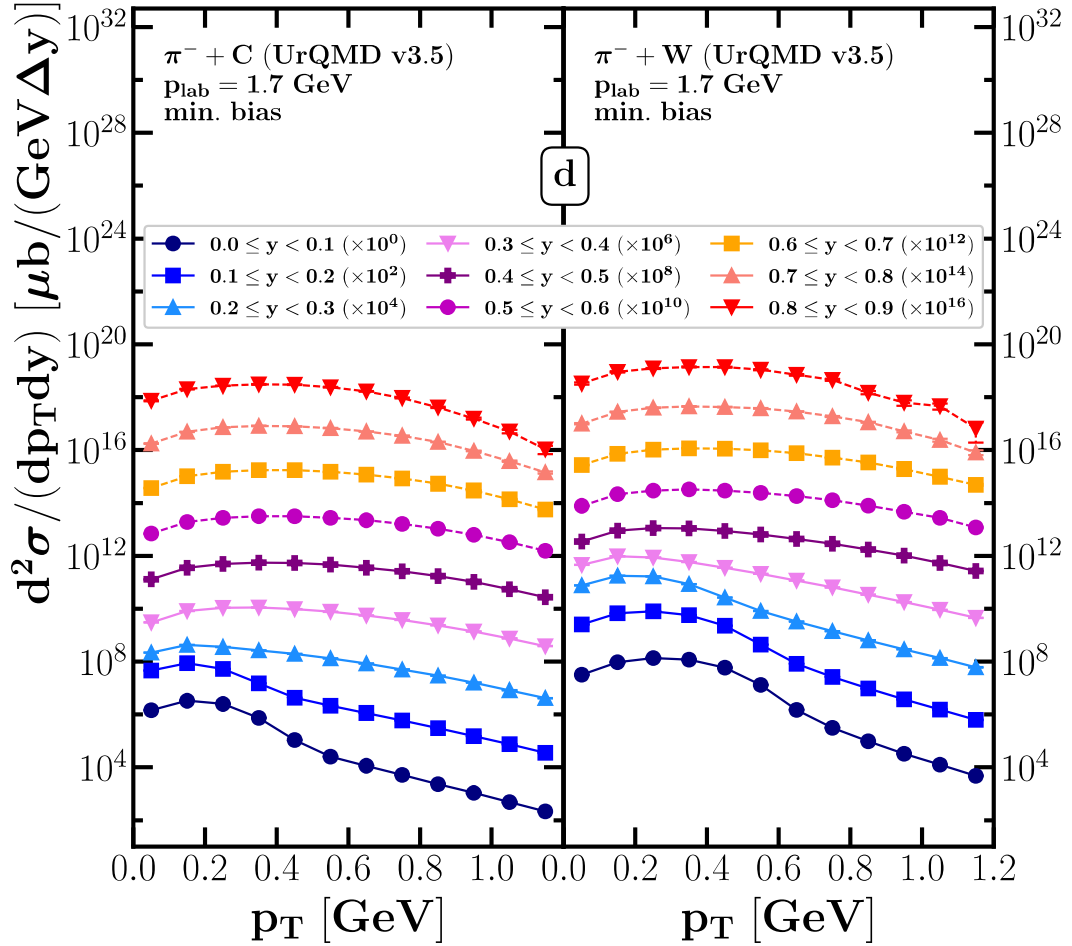


**Figure 8.5** The transverse momentum differential cross section  $d^2\sigma/dp_T dy$  in  $[\mu b/(\text{GeV}\Delta y)]$  of deuterons as a function of transverse momentum in different rapidity bins (from  $0 \leq y < 0.1$  to  $0.8 \leq y < 0.9$ , the curves are successively multiplied by factors of 100 from bottom to top) for minimum bias  $\pi^- + \text{C}$  (left panel) and  $\pi^- + \text{W}$  (right panel) collisions from UrQMD.

low  $p_T$ ) similar to the transverse momentum of protons. This effect is present in all light nuclei  $p_T$  spectra due to the mentioned effect of protons sitting inside the target. This finding suggests that the UrQMD model can effectively describe the formation of these clusters in  $\pi^- + \text{C}$  and  $\pi^- + \text{C}$  collisions.

Figure 8.8 presents the rapidity dependence of cluster yields. It shows the rapidity differential cross sections ( $d\sigma/dy$ ) in  $[\mu b/\Delta y]$  for deuterons (orange), tritons

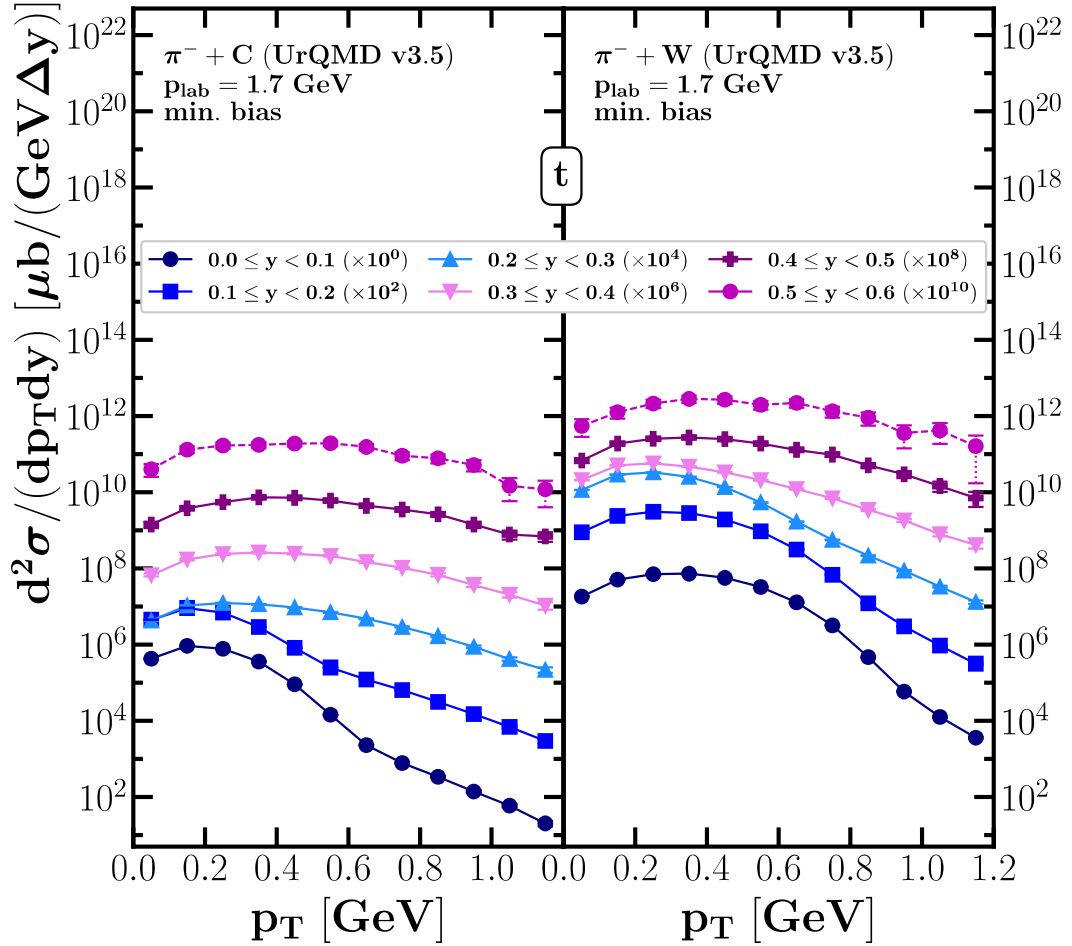


**Figure 8.6** The transverse momentum differential cross section  $d^2\sigma/dp_T dy$  in  $[\mu\text{b}/(\text{GeV}\Delta y)]$  of tritons as a function of transverse momentum in different rapidity bins (from  $0 \leq y < 0.1$  to  $0.5 \leq y < 0.6$ , the curves are successively multiplied by factors of 100 from bottom to top) for minimum bias  $\pi^- + \text{C}$  (left panel) and  $\pi^- + \text{C}$  (right panel) collisions from UrQMD.

(green),  $^3\text{He}$  (blue), and  $^4\text{He}$  (red) as a function of rapidity for both  $\pi^- + \text{C}$  and  $\pi^- + \text{C}$  collision systems. The UrQMD coalescence model results are depicted by dashed lines with open symbols, while the yields from the Statistical Multifragmentation Model (SMM) are represented by solid lines without symbols.

The overall light cluster multiplicities from both models show good agree-

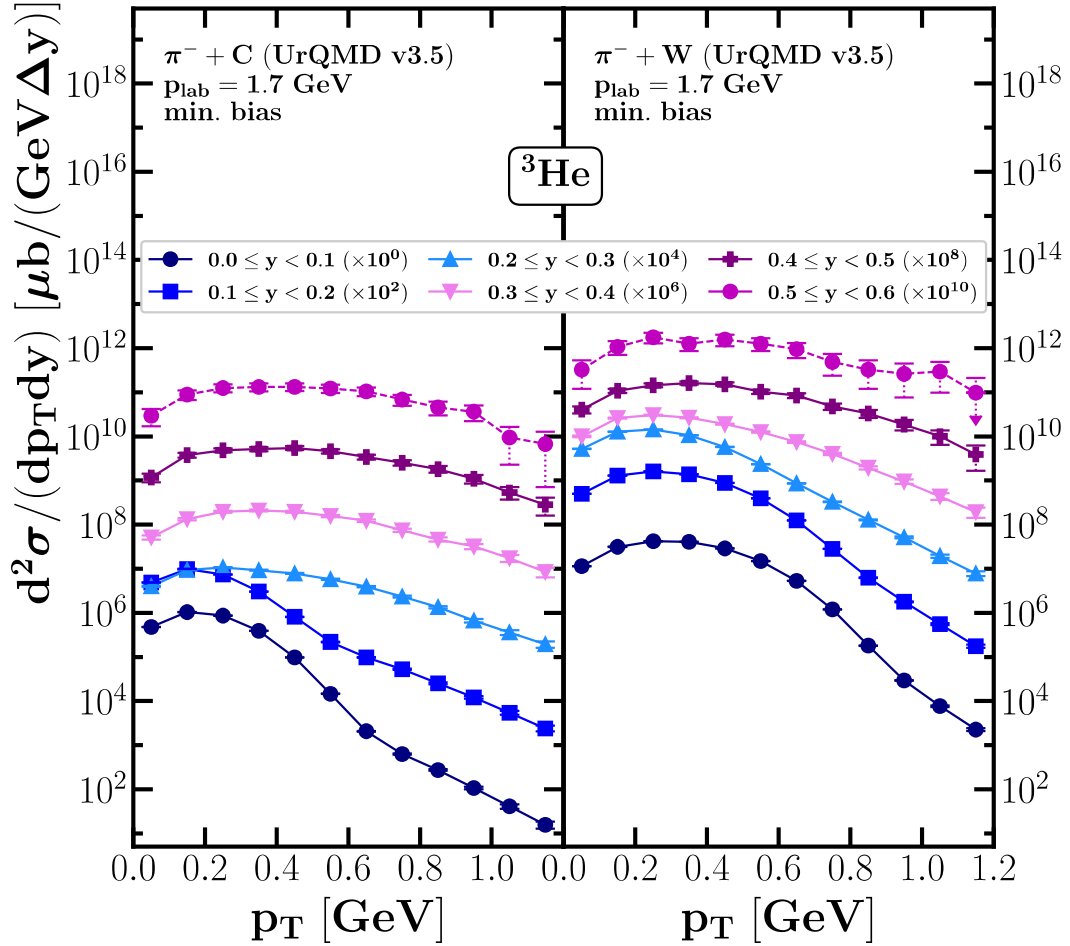


**Figure 8.7** The transverse momentum differential cross section  $d^2\sigma/dp_T dy$  in  $[\mu\text{b}/(\text{GeV}\Delta y)]$  of  ${}^3\text{He}$  as a function of transverse momentum in different rapidity bins (from  $0 \leq y < 0.1$  to  $0.5 \leq y < 0.6$ , the curves are successively multiplied by factors of 100 from bottom to top) for minimum bias  $\pi^- + \text{C}$  (left panel) and  $\pi^- + \text{C}$  (right panel) collisions from UrQMD.

ment, with a factor of two difference between  ${}^4\text{He}$  multiplicities. As expected, the cluster yields (shown in Figure 8.8) peak around zero rapidity, indicating that most clusters form in the target region where protons (nucleons) are abundant. Interestingly, both systems exhibit a protrusion in the deuteron distributions towards forward rapidity, particularly pronounced in the smaller carbon system. This suggests that the

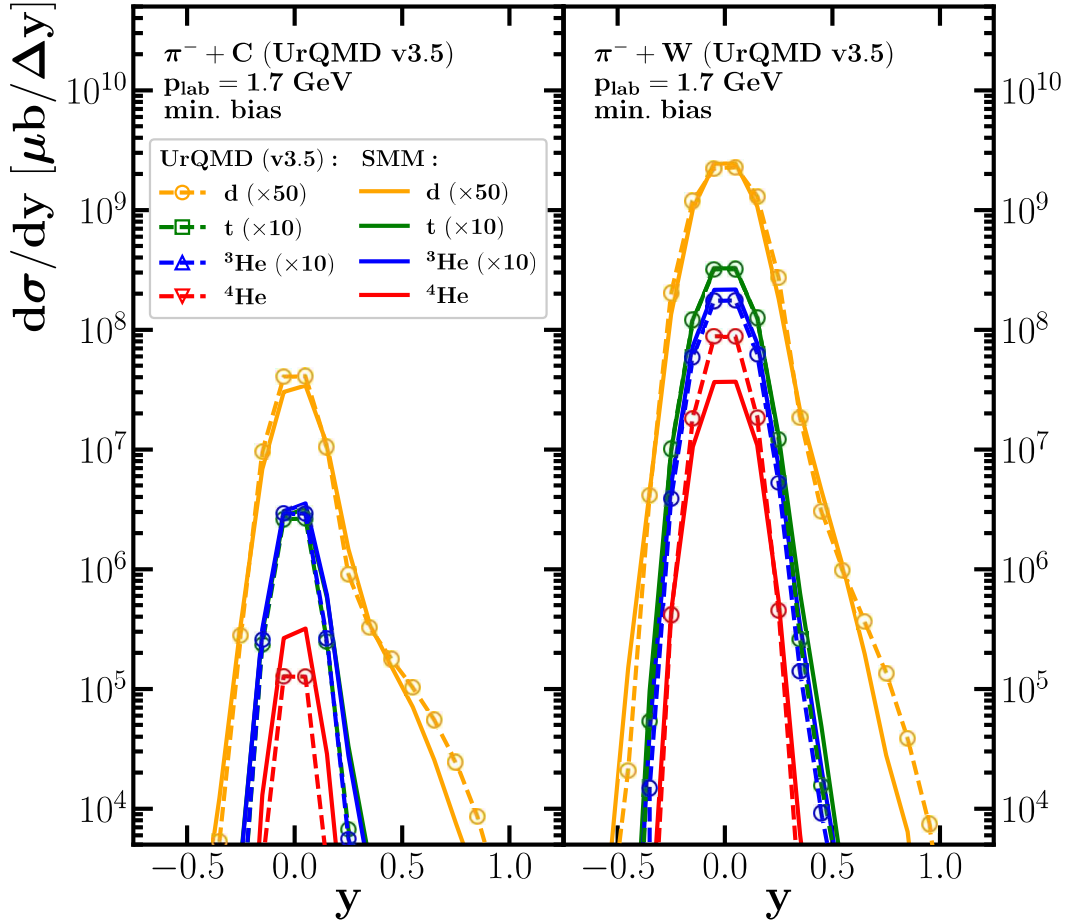


**Figure 8.8** The rapidity differential cross section  $d\sigma/dy$  in  $[\mu\text{b}/\Delta y]$  of deuterons (orange), tritons (green),  $^3\text{He}$  (blue) and  $^4\text{He}$  (red) as a function of the rapidity for minimum bias  $\pi^- + \text{C}$  (left panel) and  $\pi^- + \text{W}$  (right panel) collisions from UrQMD (v3.5) as denoted by dashed lines with symbols and from statistical multifragmentation model (SMM) as denoted by solid lines without symbols.

incident pions could occasionally eject only a few nucleons out of the target.

The tungsten target ( $\pi^- + \text{C}$ ) shows a more symmetrical deuteron distribution compared to the carbon target ( $\pi^- + \text{C}$ ). This can be explained by the concept of stopping power. The larger size and higher stopping power of the tungsten nucleus lead to more frequent coalescence and/or multifragmentation around the target region. This, in turn, enhances and broadens the rapidity distributions for all clusters in the  $\pi^- + \text{C}$

system compared to  $\pi^- + C$  washing out the protrusion effect in deuteron distribution.

## 8.5 (Hyper) Nuclei distribution

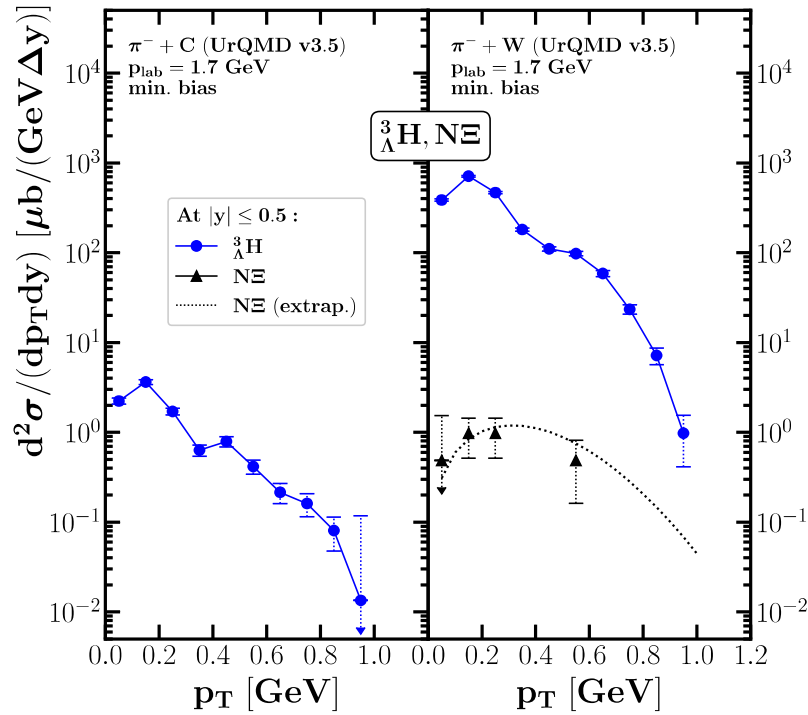


**Figure 8.9** The differential cross section with respect to transverse momentum  $d^2\sigma/dp_T dy$  [ $\mu\text{b}/(\text{GeV}\Delta y)$ ] of  ${}^3\text{He}$  (blue line with squares) and  $N\Xi$  (black triangles) from UrQMD results at mid-rapidity minimum bias  $\pi^- + C$  (left panel) and  $\pi^- + W$  (right panel) collisions. The dashed line indicates the extrapolated fit of  $N\Xi$ .

Finally, we come to the most intriguing aspect of this study discussing about the potential production of hypernuclei. Here, we focus on the hypertriton ( ${}^3_{\Lambda}\text{H}$ ) and  $N\Xi$  hypernuclei.

Figure 8.9 presents the predicted transverse momentum spectra of the hypertriton  ${}^3_{\Lambda}\text{H}$  (blue line with circles) and anticipated  $N\Xi$  clusters from UrQMD model simulations and its corresponding extrapolated fit (black triangles and dotted line respectively). The spectra show the production rates as a function of the transverse momentum ( $p_T$ ) for minimum bias  $\pi^- + C$  and  $\pi^- + C$  collisions at mid-rapidity

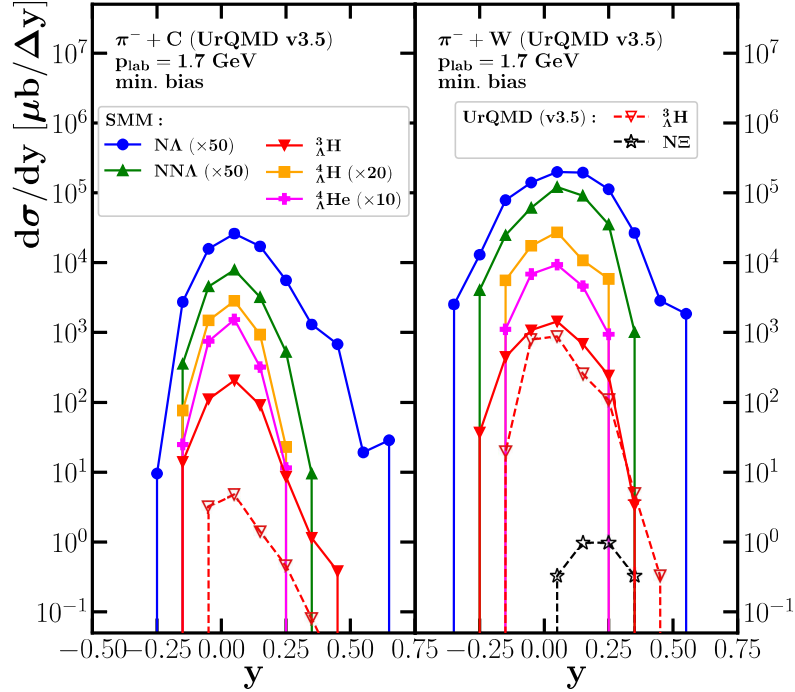


**Figure 8.10** The differential cross section with respect to rapidity  $d\sigma/dy [\mu\text{b}/\Delta y]$  of  $N\Lambda$  (blue),  $NNA$  (green),  ${}^3_{\Lambda}\text{H}$  (red),  ${}^4_{\Lambda}\text{H}$  (orange),  ${}^4_{\Lambda}\text{He}$  (pink), and  $N\Xi$  (black) from minimum bias  $\pi^- + \text{C}$  (left panel) and  $\pi^- + \text{W}$  (right panel). The UrQMD results are denoted by dashed lines with open symbols, while the results from the statistical multifragmentation model (SMM) are denoted by solid lines with full symbols.

( $|y| \leq 0.5$ ). The significant production of  ${}^3_{\Lambda}\text{H}$  suggests a high probability of detection with momenta accessible by the HADES experiment. The production and measurement of  $N\Xi$  clusters might also be achievable.

Figure 8.10 shows the predicted rapidity distributions of various hypernuclei from  $A = 2 - 4$  in SMM (solid lines and filled symbols) models contrasting with UrQMD results (dashed lines and open symbols).

The  ${}^3_{\Lambda}\text{H}$  production cross section peaks around the target rapidity region, indicating formation primarily within the target nucleus. The yield is higher and more symmetric in the  $\pi^- + \text{C}$  system compared to  $\pi^- + \text{W}$ . This is attributed to the fact that the tungsten system produces more hyperons and has a higher stopping power, effectively increasing the probability of hypernuclei formation.

In addition, the protrusion effect is also observed in the hypernuclei yield with  $A \leq 3$  from both models, i.e.,  $N\Lambda$  (blue line with circles),  $NN\Lambda$  (green line with up triangles), and  ${}^3_\Lambda\text{H}$  (SMM: red line with down triangles, UrQMD: red dashed line with down triangles). As discussed before, the incoming pions could knock out only a few nucleons toward the forward rapidity region. The agreement between UrQMD and SMM models for light cluster and hypertriton formation is good for the larger tungsten system. However, a factor of 10 difference exists for the smaller carbon system, given a potential lower and upper bound of error in hypertriton production estimates.

Quantifying these predictions, the expected yield is on the order of  $10^{-3}$  hypertritons and  $10^{-6}$   $N\Xi$  per event in these collisions. This translates to approximately  $10^5$  and  $10^2$  detectable  ${}^3_\Lambda\text{H}$  and  $N\Xi$  from the entire data set of the HADES collaboration ( $10^8$  recorded events per system) reported in Ref. (Yassine et al., 2023). This large number allows for detailed studies and measurements of the hypertriton and potentially  $N\Xi$ .

## 8.6 Fragments of larger mass numbers

To conclude our analysis, we present a compilation of estimated total abundances for normal nuclei and hypernuclei, ranging from light elements up to oxygen (mass number  $A = 16$ ). These estimates aim to quantify the production rates of various nuclei following pion beam collisions with carbon ( $\pi^- + \text{C}$ ) and tungsten ( $\pi^- + \text{C}$ ) targets at an incident momentum of  $p_{\text{lab}} = 1.7 \text{ GeV}/c$ .

Figure 8.11 showcases the integrated cross section for light nuclei (full symbols) and hypernuclei (single strange hyperon  $Y = 1$ , open symbols) as a function of their mass number ( $A$ ). The data is further categorized by the charge ( $Z$ ) of the nuclei, represented by different colors. The results are obtained from a SMM analysis of UrQMD (v3.5) simulation data for minimum bias  $\pi^- + \text{C}$  (left panel) and  $\pi^- + \text{C}$  (right panel) collisions.

The figure reveals that the abundance of both light clusters and hypernuclei follows an approximately exponential decrease with increasing mass numbers. This aligns with observations from light nuclei production at RHIC (Agakishiev et al., 2011). Despite the decline, the integrated production cross sections might still be sufficient for signal detection by the HADES collaboration or in future pion-beam experiments with higher beam luminosity.

Notably, the translated yields from the cross section for normal nuclei and

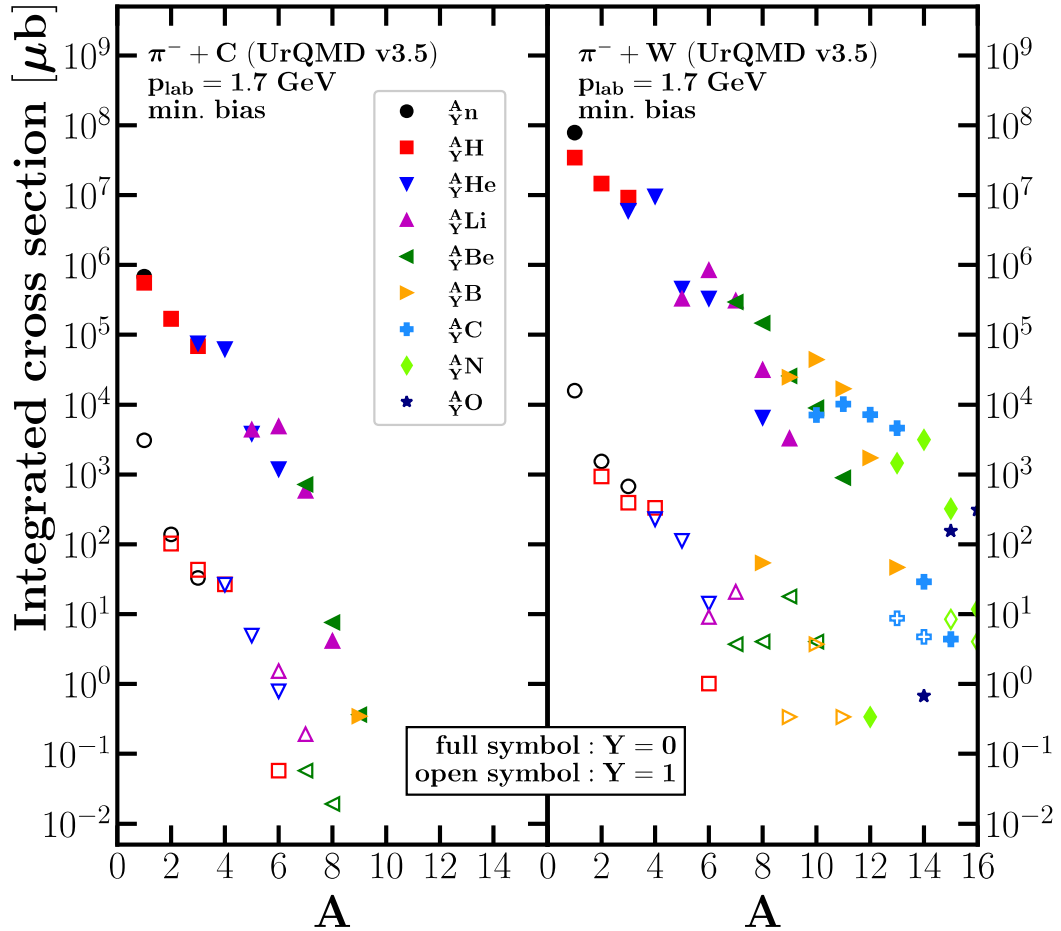


**Figure 8.11** The mass number distribution of the integrated cross section of light nuclei (full symbols:  $Y=0$ ) and hypernuclei (single-strange as open symbols:  $Y=1$ ) production with different charges  $Z$  (denoted by the color) from SMM analysis of the UrQMD data at minimum bias  $\pi^- + C$  and  $\pi^- + C$  collisions.

hypernuclei remain at the level of  $10^{-4}$  to 1 and  $10^{-6}$  to  $10^{-3}$  per event, respectively. This paves the way for the first-ever exploration of normal clusters and hypernuclei with mass  $A > 4$  in pion beam collision experiments.

Furthermore, as reported by the HADES collaboration Ref. (Ardid et al., 1999), their pion beam can reach momenta of up to 2.5 GeV. This higher beam energy is expected to significantly increase the production cross sections, potentially enabling

the study of  $\Xi$ -hypernuclei as well. This opens an exciting opportunity to explore aspects of hypermatter physics within the HADES  $\pi + A$  program, potentially mirroring some of the objectives envisioned for the PANDA experiment.

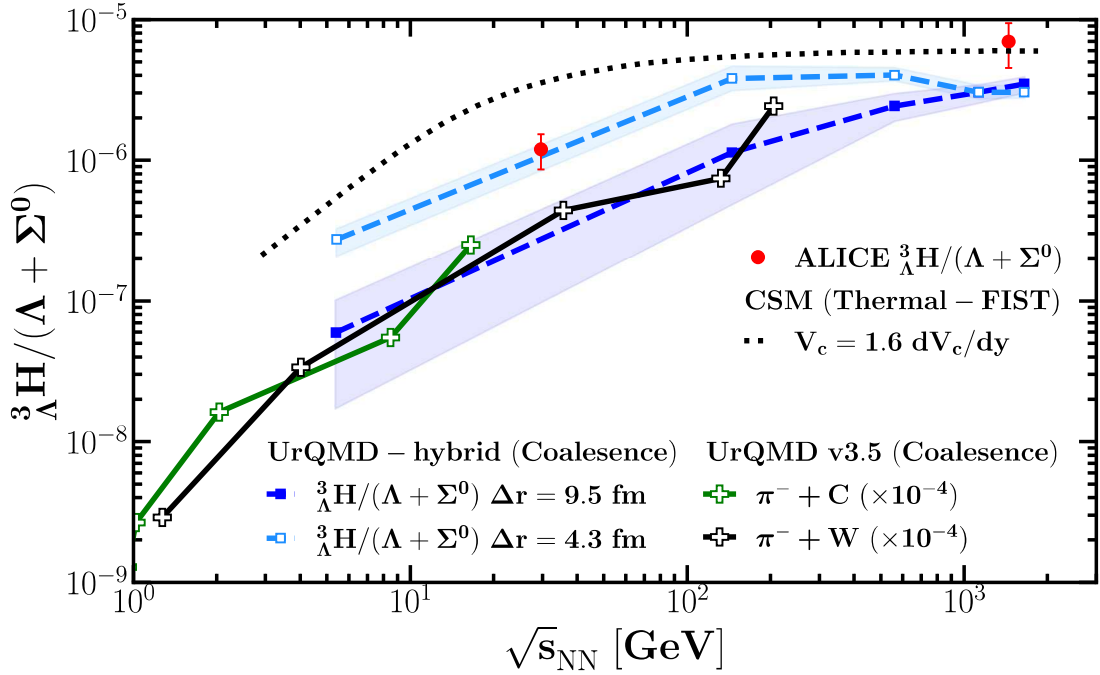


**Figure 8.12** The comparison in the yield ratio of the hypertriton ( ${}^3_{\Lambda}\text{H}/(\Lambda + \Sigma^0)$ ) as a function of the mean charged particles multiplicity with various models. Our analysis for  $\pi^- + \text{C}$  (green line) and  $\pi^- + \text{C}$  (black line) is presented alongside data from p+Pb and Pb+Pb. The figure also includes predictions from two models: the thermal-statistical model denoted by CSM Thermal-FIST (dotted line) (Vovchenko et al., 2018a) and the previous UrQMD-hybrid coalescence model (coloured lines with symbols (Sun et al., 2019)). Finally, brown diamonds represent experimental measurements by the ALICE collaboration (Acharya et al., 2022).

The integrated yields of hypertritons ( ${}^3_{\Lambda}\text{H}$ ) and  $(\Lambda + \Sigma^0)$  hyperons allow for an analysis of the dependence on collision system size. Centrality classes are approximated by the proton multiplicities. Figure 8.12 presents the results.

The analysis aligns well with previous findings from the UrQMD-hybrid coalescence model (coloured line with squares) for larger systems, exhibiting a suppression of hypertriton yield ratio towards smaller systems. This  $\pi^- + A$  study indeed enables predictions for the yield ratio behavior at even lower system sizes. Interestingly, for smaller systems ( $dN_{\text{ch}}/d\eta < 10$ ), the hypertriton yield ratio from  $\pi^-$ -reactions shows

an even stronger suppression compared to the thermal model (dotted line), which fails to capture this effect even at the p+Pb volume. While the p+Pb experimental data agrees with the moderate suppression predicted by the coalescence parameter  $\Delta r = 4.3$  fm, i.e., smaller hypertriton wavefunction, the overall trend supports the coalescence model's formation mechanism.

However, our predictions suggest a larger hypertriton wavefunction with a coalescence parameter of  $\Delta r = 9.5$  fm. This indicates a potentially more extended wavefunction due to a loosely bound d-core with the  $\Lambda$  hyperon. Future HADES experiments with higher precision could validate these predictions and provide further insight on the formation mechanism.

This chapter explores the formation of clusters and hypernuclei in  $\pi^- + A$  at the HADES experiment. Studying these collisions offers a unique opportunity allowing us to investigate cluster formation in regimes where there is limited experimental data, particularly for smaller systems.

The first step involved validating our simulation model. We employed the UrQMD model to simulate  $\pi^- + C$  and  $\pi^- + C$  at momentum of  $p_{\text{lab}} = 1.7$  GeV/c. The simulated results, including the transverse momentum and rapidity distribution of protons and  $\Lambda$ 's, show good agreement with experimental data from the HADES experiment. However, we identified a limitation in HADES acceptance to capture low  $p_T$  protons near the target region. This suggests a need for adjustments to the exponential function used.

We then proceed to investigate the production of deuterons, tritons,  $^3\text{He}$ , and  $^4\text{He}$  nuclei. We compare two different theoretical approaches between the coalescence model and the Statistical Multifragmentation Model (SMM). Both approaches successfully reproduced the observed spectra of light clusters, with good agreement in their rapidity distributions. Interestingly, both models also show a protrusion in the distribution of deuterons towards forward rapidity. This suggests that incoming pions only knock a few nucleons out of the target nucleus. Furthermore, the larger tungsten target system results in broader rapidity distributions for all clusters compared to the carbon target. This can be attributed to the stronger stopping power of tungsten, which leads to a higher probability of binding and multifragmentation at kinetic freeze-out.

Building upon the success with light nuclei, we investigated the production of hypernuclei. Similar to light clusters, hypernuclei with a mass number  $A < 3$  displayed a protrusion towards forward rapidity as well as broader rapidity distributions for all

hypernuclei in the tungsten system. We then estimated the total abundances for all clusters, including both normal nuclei and hypernuclei up to oxygen mass. These estimates suggest that the yields are sufficiently high to be detectable by the HADES collaboration.

Finally, we explored potential avenues for future research and investigated the system size dependence of hypernuclei. Our analysis of the yield ratio of hypertriton as a function of charged multiplicity revealed a strong suppression in  $\pi^- + A$  collisions compared to the thermal model. This finding supports the coalescence model with a larger hypertriton wavefunction (coalescence parameter  $\Delta r = 9.5$  fm).

In conclusion, this chapter highlights the potential of using pion-nucleus collisions at low energies and smaller system sizes to study cluster formation and hypernuclei production. The good agreement between simulations and experimental data paves the way for further exploration of hypermatter physics using the HADES pion-induced program. We propose that using a higher momentum pion beam in the HADES setup could enable studies of the production of  $\Xi$  hyperons via the decay of a resonance state (Steinheimer and Bleicher, 2016). This approach might also allow for the investigation of the formation of double- $\Lambda$  hypernuclei.